

**1 Wind Veer and Speed in Turbulent Ekman Flow - Part 1:
2 Scaling analysis and universal profile model**

3 Cedrick Ansorge¹ and Hauke Wurps²

4
5 Submitted August 5, 2024

6 Abstract

7 The profiles of wind speed and direction in turbulent Ekman flow are formulated
8 based on asymptotic theory and data from direct numerical simulation. The profile
9 of the streamwise component follows the classical viscous, logarithmic and wake
10 scaling. In the outer layer, the velocity component profiles can be described by an
11 Ekman-spiral with adapted boundary conditions that result in a reduction of the
12 spiral-like rotation. The span-wise component poses a conceptual challenge to the
13 channel-flow analogy in the context of asymptotic matching; it exhibits a mixed
14 scaling in the surface layer, but follows outer scaling for most of the outer layer.
15 Viscous stress scales universally across the boundary layer in inner units while
16 the total stress becomes universal as a function of outer height. This implies a
17 mixed scaling for the turbulent stress and eddy viscosity across the inner layer
18 and convergence to a universal scaling as function of the outer height across the
19 outer layer for increasing scale separation vide Reynolds numbers.

20 1 Introduction

21 The Coriolis force bends the path of motion on a rotating sphere and establishes
22 geostrophic equilibrium when in balance with a pressure gradient force. Wind veer
23 away from the wind direction in geostrophic equilibrium is (i) due to direct fric-
24 tional effects in the very vicinity of the surface and (ii) due to turbulence which
25 exerts indirect frictional effects; these effects cause a slow-down of the mean wind
26 reducing the Coriolis force thus turning the wind in favor of the pressure gradient
27 force. Not only does the veering set the frame of reference for surface layer theory,
28 it also has effects at small and large scales from large-scale dispersion via plume
29 spreading to cyclone spin-down (Svensson and Holtslag 2009) and on the capa-
30 bilities of data assimilation and accuracy of surface flux estimates (Brown et al.
31 2005). From a large-scale perspective, the veering of wind across the planetary

¹ FU Berlin, Institut für Meteorologie, Carl-Heinrich-Becker-Weg 6–10, 12165 Berlin
cedrick@posteo.de

² Uni Oldenburg

boundary layer determines the amount of cross-isobaric mass-flux, commonly referred to as 'Ekman pumping' (Ekman 1905), and it is thus a key factor in the life-cycle of large-scale synoptic systems. Within the atmospheric boundary layer (ABL), directional shear of the wind in the upper part of the surface layer may cause a systematic yaw for tall wind power generation devices where blades reach into the Ekman layer, i.e. that part of the boundary layer where the wind starts to turn; an exact estimate of such effects is critical in the site assessments for wind farms (Calaf et al. 2010; Mirocha et al. 2018).

In the planetary boundary layer, wind veer is characterized by the surface veering angle α defined as the angle between the negative surface shear stress τ_{sfc} and the geostrophic wind. Surface veering α and geostrophic drag $Z \equiv u_*/G$, where the friction velocity $u_* \equiv \sqrt{|\tau_{\text{sfc}}|/\rho}$, uniquely determine the surface drag τ_{sfc} in a turbulent Ekman flow. In any quantitative description of the surface layer, the friction velocity u_* is the dynamic scale and α defines the alignment of the frame of reference. Knowledge about u_* and α is thus a prerequisite for any quantitative theory of the surface layer, and Rossby and Montgomery (1935) constrained the two parameters based on integral relations in the ABL. Asymptotic similarity theory was later used by Tennekes (1973); Blackadar and Tennekes (1968), and—based on his seminal direct numerical simulations (DNS) of Ekman flow—, Spalart (1989) suggested a modification to take into account effects of low to intermediate Reynolds numbers. Later on, constants were re-evaluated with a focus on the ABL based on observations (Högström 1988, 1996) and numerical modelling (Spalart et al. 2008, 2009; Ansorge and Mellado 2014; Ansorge 2019).

Attempts were also undertaken to obtain profiles of the wind speed: One approach is to match the inner and outer layer at a reference height; Etling (2002); Emeis (2018) (Sec. 21.10; Eq. 21.48) choose the Prandtl-layer height z_{Prandtl} to match the wind speed profiles, which, however, requires external prescription of $\alpha(z_{\text{Prandtl}})$, the veering at that height. A one-dimensional profile with constant veering is given by Emeis et al. (2007, Sec. 3; Eq. 3.1-3.19).

Gryning et al. (2007) present an extension of the wind-speed profile beyond the surface layer using a neutral reference profile and a stability correction; Kelly and Gryning (2010), based on a probabilistic representation of stratification, develop a model for the long-term mean wind speed in the ABL and compare this with observation at different sites; Kelly and Troen (2016) demonstrate the effect of such improved model for wind-energy applications. In consideration of the large scale separation in geophysical flow, the rotation of the wind in the surface layer is often assumed negligible, and above investigations merely focus on the wind speed; that means, the veering of the wind with height is not described and there is little knowledge on the profile of the span-wise velocity component and the precise shape of the hodograph in the limit of a truly neutral Ekman boundary layer. A climatology of wind turning in the ABL is given by Lindvall and Svensson (2019) Klein et al. (2021) use a statistical turbulence modelling approach that yields a two-component velocity profile, but they also find that the exact representation of turning is challenging.

Ekman-layer models are roughly based on Ekman's seminal 1905 paper in combinations with additional assumptions, such as a prescribed profile shape for eddy viscosity Ellison (1955) and two-layer models of the ABL take into account rotational effects at higher altitudes, for instance when the wind speed needs to be evaluated at heights on the order of 100 – 200 m, a particular concern when

it comes to wind-power forecasting (Optis et al. 2014). Despite rotational effects being considered, the formulation of these models for the outer layer and analysis of their performance primarily focuses on wind speed. Still, in 2018, Jiang et al. recognized that the outer part of the Ekman boundary layer receives less attention in comparison with the surface layer and study the neutral problem by Large-Eddy simulation (LES). They focus on the wind speed and find an extended logarithmic layer when considering the wind speed instead of the shear-aligned component, and they eventually demonstrate by means of an analytical model that this vertical extension of the logarithmic layer may be explained by a transfer of stress to the span-wise velocity component where it is assumed that the shear vector $\tau(z)$ and stress vectors $(\partial_z U, \partial_z V)$ are aligned.

More recently, Ghannam and Bou-Zeid (2021) treated the horizontally averaged momentum budget to show that departures from shear-alignment in the vicinity of the surface result in an integral of the wind veer (α_M in their notation) over the height to very high accuracy ($\int_{z_0}^H \sin \alpha_M$ in their notation; their Eq. (16)). Classic surface-layer similarity is recovered when the angle α_M does not depend on height, i.e., the wind veer is constant across the surface layer. If, however, the wind veer depends on height, the profiles of stress and mean velocities depart from the scalings implied by classic surface-layer similarity.

Turbulent Ekman flow is considered here as a conceptual model of the homogeneous, stationary ABL over a flat surface under neutral stratification. Universal profiles of the wind vector for turbulent Ekman flow not only are a well-described limit for theoretical exploration or higher-order approaches taking into account possible effects of stratification, roughness or other physical complications encountered in the real geophysical system. While, on first sight, the study of such a strongly idealized case appears as an academic problem, it contains the essence of surface similarity as it is used in most atmospheric models, be it conceptual or numeric ones. More complex accounts generally refer to the homogeneous stationary problem as a base state: (i) Roughness is commonly incorporated by a linear transformation of vertical scale involving the roughness parameter z_0 and for larger roughness also a displacement height (Monin and Yaglom 1975; Jacobs and Van Boxel 1988; Högström 1988); (ii) Stability can be accounted for by a linearization around the neutrally stratified profile (Monin 1970; Monin and Yaglom 1975; Högström 1988, 1996; Sakagami et al. 2020); (iii) Non-stationarity in the pressure-gradient forcing can be accounted for by a linear damped-oscillator approach around the base state (Momen and Bou-Zeid 2016); (iv) Barotropic and baroclinic effects on the velocity profile require to consider the height-dependence of the veer and stress misalignment (Momen et al. 2018; Ghannam and Bou-Zeid 2021). Furthermore, such a solution can serve as better initial condition for numerical simulation of the flow, to minimize the length of initial transient periods, or as benchmark for turbulence closures that can be tuned to reproduce the neutral limit case.

Despite the strong simplifications implied by our choice of set-up, there is no straightforward approach to solving this well-defined problem. Large-Eddy simulation not only needs to be tuned for the surface shear stress and veering angle, but it also relies on sub-grid closures that commonly assume alignment of the turbulent stress with gradients. This pre-requisite is not fulfilled when the wind rotates with height. Esau (2004) investigated the representation of the Ekman boundary

layer by dynamical subgrid closures and Zikanov et al. (2003) proposed a closure for the wind profile using a linearized representation of the eddy viscosity. Despite advances in analysis of this simplified set-up (Jiang et al. 2018), there is yet insufficient understanding for a quantitative generalization of the results to arbitrary external forcing (manifest in variation of the Reynolds number) – and indeed the fundamental questions pertaining to such relatively simple dynamics of turbulence are not reflected in the research on LES for the ABL over the past 50 years (Stoll et al. 2020).

At the same time, an increasing amount of high-quality and high-resolution data from turbulence-resolving approaches is emerging due to recent advances in high-performance computing and its application to geophysical problem sets; the geophysical range of scale separation, however, is—and it will remain so for the foreseeable future—out of reach for such simulation (Dimotakis 2005). Here, the routinely employed concept of Reynolds-number similarity can help. It postulates the existence of *fully developed turbulence* believed to occur for a sufficiently large but finite Reynolds number (Barenblatt and Goldenfeld 1995). (Already in 1998, this in fact lead Moin and Mahesh to the question *how high a Re is high enough?*) Certain statistics of fully developed turbulence, such as dissipation (Dimotakis 2005) or profiles of mean velocity (Barenblatt 1993), become independent of the Reynolds number when appropriately scaled; other statistics, such as the near-wall maximum in velocity fluctuation depend on Re (Baars and Marusic 2020) and externality of the flow may exert an impact on near-wall scaling (da Silva et al. 2014). It appears that for certain statistics in Ekman flow, fully-developed turbulence is reached with the Reynolds numbers that became possible due to an increase of computing capabilities over the past decades.

This paper exploits the robust features of mean velocity profiles from direct numerical simulation across a range of Reynolds numbers to formulate both the streamwise and span-wise components of the mean velocity vector as a function of the Reynolds number.

158 2 Problem Formulation and Numerical Approach

We consider here incompressible, turbulent Ekman flow, that is, the turbulent flow over a flat rotating plate, as a physical model for the truly neutral ABL. The f-plane approximation is applied such that rotation only acts on horizontal velocity components; we thus neglect rotational effects on the horizontal components of velocity and dynamical effects due to latitudinal variation of the rate of rotation.

164 2.1 Notation and Governing Equations

The dimensional velocity vector of the numerical simulations is $\underline{U} = (U_1, U_2, U_3) = (U, V, W)$ over the coordinate system $Oxyz$, where an approximate alignment (plus/minus few degrees) of the direction Ox with the surface shear stress is achieved. The coordinate Oz points away from the wall, and Oy points in the span-wise direction normal to Oxz . For analysis of the results, we use two coordinate systems that are

170 (i) exactly aligned with the surface shear stress

$$\underline{\tau}_{\text{sfc}} = \begin{pmatrix} \tau_x \\ \tau_y \\ \tau_z \end{pmatrix} = -\nu \left(\frac{\partial U}{\partial z} \hat{e}_x + \frac{\partial V}{\partial z} \hat{e}_y \right) \quad (1a)$$

171 and labelled by an upper index α as in \underline{U}^α for the velocity vector, and (ii) the
 172 coordinate system aligned with the free-atmosphere geostrophic wind labelled by
 173 an upper index G as in \underline{U}^G . We denote the modulus of the surface shear, the
 174 surface friction, by

$$u_* = \sqrt{\|\underline{\tau}_{\text{sfc}}\|} \quad (1b)$$

175 and let $Z_* = G/u_*$; the surface veering angle α_* is the angle between $\underline{\tau}$ and the
 176 geostrophic wind

$$\alpha_* = \sphericalangle(\underline{G}, \underline{\tau}_{\text{sfc}}). \quad (1c)$$

177 Analogously, we denote the height-local veering of the wind $\alpha(z) = \sphericalangle(\underline{G}, \underline{U}(z))$,
 178 where $\underline{G} = (G_1, G_2, 0)$ is the geostrophic wind vector.

179 We consider the incompressible Navier–Stokes equations for the three velocity
 180 components on the f-plane in a framework that is governed by (i) geostrophic wind
 181 magnitude $G = \sqrt{G_1^2 + G_2^2}$, (ii) Coriolis parameter f (representing the angular
 182 rotation), and (iii) kinematic viscosity ν . In absence of external variability, this
 183 system converges to a statistically steady state in the sense that flow statistics
 184 do not depend on time; and this state is defined by a Reynolds number, the only
 185 non-dimensional parameter that governs the system. We use the geostrophic wind
 186 as velocity and the Coriolis parameter f as time scale for the non-dimensional
 187 framework. This implies the Rossby radius $A_{\text{Ro}} = G/f$ as length scale, such that
 188 one Reynolds number governing the problem reads as

$$\text{Re}_A = \frac{GA_{\text{Ro}}}{\nu}. \quad (2)$$

189 The scales used in defining Re_A are of limited relevance for description of the
 190 turbulent flow state. The turbulence scale separation in a wall-bounded flow is
 191 commonly characterized by the friction Reynolds number (Jiménez 2012):

$$\text{Re}_\tau = \frac{u_* \delta}{\nu} = \delta^+ = \frac{\text{Re}_A}{Z_*^2}, \quad (3)$$

192 where $\delta = u_*/f$ and we use a superscript '+' to denote normalization by inner
 193 turbulence scales (u_*, ν) . Another common measure of scale separation is the
 194 Reynolds number defined by the laminar Ekman layer thickness $D = \sqrt{2\nu/f}$,

$$\text{Re}_D = \frac{GD}{\nu} = \sqrt{2\text{Re}_A}. \quad (4)$$

195 Another common measure of scale separation is the Reynolds number defined by
 196 the laminar Ekman layer thickness $D = \sqrt{2\nu/f}$,

$$\text{Re}_D = \frac{GD}{\nu} = \sqrt{2\text{Re}_A}. \quad (5)$$

197 The governing equations non-dimensionalized by G , f , and Λ_{Ro} read as

$$\frac{\partial u_i}{\partial t} = \frac{\partial \pi}{\partial x_i} - u_j \frac{\partial u_i}{\partial x_j} + \epsilon_{i2j}(u_j - G_j) + \frac{1}{\text{Re}} \frac{\partial^2 u_i}{\partial x_j^2} \quad (6a)$$

$$\frac{\partial u_j}{\partial x_j} = 0, \quad (6b)$$

198 where $u_i = U_i/G$ are the non-dimensional components velocity, π is non-dimen-
199 sional pressure, $g_j = G_j/G$ are non-dimensionalized components geostrophic wind
200 (with $g_1^2 + g_2^2 = 1$ by construction), and ϵ is the Levi–Civita tensor. These equations
201 are solved inside a bounded cube of size $L_x \times L_y \times L_z$ with periodic boundary condi-
202 tions in the lateral (streamwise and spanwise) directions, a no-slip–no-penetration
203 boundary at $z = 0$, and a no-penetration, free-slip boundary at $z = L_z$.

204 2.2 Numerical Simulations

205 The problem is solved numerically by tLab¹, an open-source tool-suite to simulate
206 and analyze turbulent flows. We use here a fourth-order–five-step Runge–Kutta
207 integration and sixth-order compact schemes for spatial derivatives in all direc-
208 tions. The incompressibility constraint is enforced by a fractional step approach
209 where the Poisson equation for the pressure field is solved to machine accuracy
210 using a combined spectral/compact approach as described in Mellado and Ansorge
211 (2012).

212 Simulations used here are shown in Tab. 1. We extend an existing set of simula-
213 tions for $\text{Re}_A \in \{125\,000; 281\,250; 500\,000\}$ (gray shading; cf. Ansorge and Mellado
214 2014, 2016) by new simulations at higher Reynolds numbers up to $\text{Re}_A = 1.28 \times 10^6$
215 with a horizontal domain extent up to 3.3×10^4 viscous units. In total, this yields
216 one order of magnitude variation in terms of the scale separation in the boundary
217 layer.

218 3 Scaling behavior of the flow for Re_τ up to 3000

219 The generalization of profiles to arbitrary Reynolds numbers requires sufficient
220 scale separation in the simulations, not only to quantify the effect of the Reynolds
221 number on low-order flow statistics, but also to assess the corresponding rate-of-
222 change to eventually allow for an extrapolation of the findings. While the simula-
223 tions previously available (gray shading in Tab. 1) give confidence in a first-order
224 representation of the turbulent problem, the estimation of higher-order effects such
225 as the dependency of the Reynolds number requires a broader scale separation that
226 is made available by the two new simulations at increased Reynolds number (cf.
227 Tab. 1). Data at such scale separation has been obtained previously (cf. Spalart
228 et al. 2008, 2009), but we also need high confidence with respect to the convergence
229 of simulation data for slow oscillations and with respect to sampling convergence,
230 which translates to two further requirements on the data: First, data should be free

¹ <https://github.com/turbulencia/tlab>

Table 1 Direct numerical simulation data sets used in this work. Re_A and Re_D refer to the Reynolds number defined in terms of the Rossby radius Λ and Ekman-layer thickness D respectively. L_{xy} is the domain size in the stream- and span-wise direction. The grid is given by the number of grid points in the stream-wise (N_x), span-wise (N_y) and vertical (N_z) directions respectively. The resolution in the span-wise and stream-wise directions are given as Δx^+ and Δy^+ . The grid in the vertical is stretched, and resolution at the wall is given by Δz^+ .

Re_A	Re_D	L_{xy}/Λ	$N_x \times N_y \times N_z$	Δx^+	Δy^+	$\Delta z^+ _{z=0}$
125 000	500	1.08	$2048 \times 2048 \times 192$	4.1	4.1	1.05
281 250	750	1.08	$3072 \times 3072 \times 384$	5.6	5.6	1.60
500 000	1 000	1.08	$3072 \times 6144 \times 512$	9.3	4.7	1.14
845 000	1 300	0.54	$2560 \times 5120 \times 640$	8.9	4.5	0.99
1 280 000	1 600	0.54	$3860 \times 7680 \times 960$	8.6	4.3	1.00

Table 2 DOIs and reference to the openly accessible data set at refubium repository

Re_D	DOI	Reference
500	10.17169/refubium-42505	Ansorge (2024a)
1000	10.17169/refubium-42507	Ansorge (2024b)
1300	10.17169/refubium-42508	Ansorge (2024c)
1600	10.17169/refubium-42509	Ansorge (2024d)

of artifacts from long-term oscillations across the vertical extent of the domain—primarily, simulations should be free of effects originating from the inertial oscillation; this is achieved here by replacing the mean value of the three-dimensional velocity fields by the time mean over a whole inertial oscillation. Second, high accuracy is also needed in terms of the statistical convergence of averages, bulk measures and large-scale structures; this requires a domain size $L_x > \mathcal{O}(\delta_{95})$. We use here $L_x = L_y = 1.08\Lambda$ for cases with $Re \leq 1000$ and $L_x = L_y = 0.54\Lambda$ for $Re \geq 1300$ which corresponds to $L_x/\delta_{95} \approx 25$ for $Re_D = 500$ and $L_x/\delta_{95} \approx 18$ for $Re_D = 1300$.

Bulk parameters of the simulations are given in Tab. 3. The surface stress is characterized by u_* and α_* in relation to the geostrophic wind vector and discussed in more detail as the drag law below in Sec. 4.1 (we find the expected slight decrease of u_* and α_* with increasing Re). The boundary-layer height estimated from the 95% stress reduction, δ_{95} , is around 0.6δ to 0.66δ . Interestingly, the integrated TKE $\int_0^\delta edz$ stays constant when normalized by the friction velocity u_* while the integrated dissipation $\int_0^\delta edz$ exhibits inviscid scaling when normalized by the magnitude G of the geostrophic wind. (TKE and dissipation normalized as $fG^{-3} \int edz$ and $u_*^{-3} \int edz$, exhibit substantial dependence on Re for the variation of u_* .) This indicates that the bulk dissipation is governed by the forcing G -irrespective of Re . Changes in Re , however, affect the level and organization of turbulence, and the parameter representing this dependency is the friction velocity u_* which describes the turbulence production processes in the surface layer, in particular in the buffer layer.

Velocity profiles in inner units ($U^+(z^+)$, Fig. 1a) and outer units ($U^-(z^-)$, Fig. 1b) are in accordance with previous work (Coleman et al. 1992; Spalart et al. 2008, 2009; Ansorge and Mellado 2014; Ansorge 2019): The profiles of the shear-aligned streamwise velocity component are well-collapsed for $Re_D > 500$ below $z^- \approx 0.15$ (circles in Fig. 1a); the case with $Re_D = 500$ is only transitionally

Table 3 Bulk characterization of the simulations for different Reynolds numbers Viscous Reynolds number Re , friction Reynolds number Re_τ , friction velocity u_* , surface veering angle α_* , normalized boundary layer depth δ_{95}/δ , inner normalization of vertically integrated TKE, outer normalization of vertically integrated dissipation.

Re	$\delta^+ = \text{Re}_\tau$	u_*	α_*	δ_{95}/δ	$f u_*^{-3} \int_0^\delta \epsilon dz$	$G^{-3} \int_0^\delta \epsilon dz$
500	479	0.0619	25.5	0.66	0.88	1.31
750	886	0.0561	21.0	0.65	0.90	1.34
1000	1403	0.0530	18.8	0.62	0.92	1.30
1300	2122	0.0501	17.9	0.59	0.85	1.24
1600	2978	0.0482	17.2	0.61	0.91	1.21

turbulent and there is no distinct inner-outer scale separation. The logarithmic law is appropriate for $50 < z^+ < 0.15 \text{Re}_\tau$, where $z^+ = \text{Re}_\tau z^-$. While the profiles $U^{\alpha*+}(z^+)$ diverge between different Re beyond $z^- = 0.15$, the corresponding profiles of the velocity deficit $(U^{\alpha*}(z^-) - G_1^\alpha)/u_*$ agree closely, irrespective of Re . This illustrates the inner–outer scale-duality in this external flow with inner scaling being appropriate in the inner layer and outer scaling in the outer layer. Also in the outer layer of the flow, u_* (and not the magnitude of the geostrophic wind G) governs the inviscid normalization, i.e. a scaling independent of the Reynolds-number.

No collapse is found for the profiles of spanwise velocity when considered in inner units, $V^{\alpha*+}(z^+)$. When normalized in outer units, the deficit profiles of spanwise velocity $(V^{\alpha*}(z^-) - G_2^\alpha)/u_*$ agree well beyond $z^- \approx 0.3$. This is a much higher level in comparison with the streamwise component that collapses also within the overlap layer, i.e. much closer to the surface (circles in Fig. 1b). The value of $V^{\alpha*+}(z^-) - G_2^\alpha$ is sensitive to the wind veering for $z \rightarrow 0$ as—for use of the shear-aligned component—it has to approach the value $-G_2^\alpha = |G| \sin \alpha \neq 0$ in view of the no-slip boundary condition. While low-Re effects appear to be present for $\mathcal{O}(\text{Re}) < 10^3$, the spanwise component converges to an Re -independent limit within the range of scale separation considered here, i.e.

$$G_2^\alpha/u_* = Z_* \sin \alpha \rightarrow \text{const. for } \text{Re} \rightarrow \infty, \quad (7)$$

which has indeed already been found by Spalart (1989), who estimates the constant from an integral relation.

The viscous stress

$$S_{\text{visc}} = \nu \sqrt{\left(\frac{\partial U}{\partial z} \right)^2 + \left(\frac{\partial V}{\partial z} \right)^2} \quad (8a)$$

exhibits universal scaling when considered as $S_{\text{visc}}^+(z^+)$ (Fig. 2a); this normalization is also appropriate in the outer layer where the viscous stress is, however, small. Small deviations from the universal profile are observed for the smallest Reynolds number $\text{Re} = 500$; we attribute these to low-Re effects in the only transitionally turbulent flow ($\text{Re}_\tau = 479$). In contrast to the viscous stress, the total stress follows outer normalization, i.e. $S^+(z^-)$ is universal; a discrepancy in the inner layer does not occur as the total stress is approximately constant in the viscous and buffer layer, and a rescaling of the height would have no effect there;

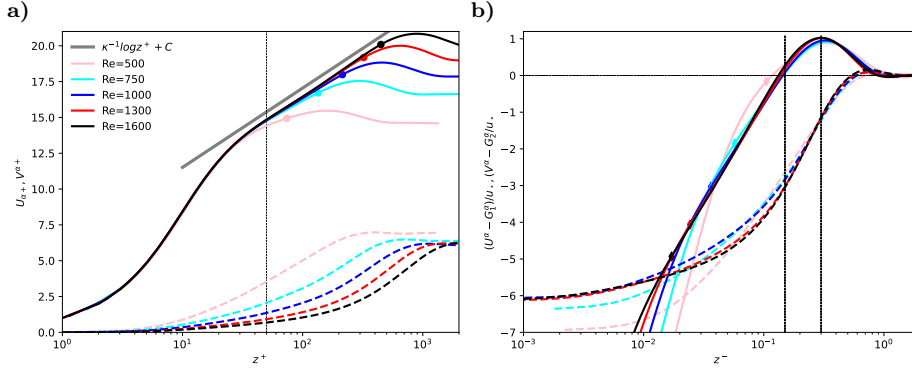


Fig. 1 a) Shear-aligned velocity profiles in inner units; b) Shear-aligned velocity deficit in outer units; circles mark the height $z^- = 0.15$; dashed line gives the best logarithmic fit to the data.

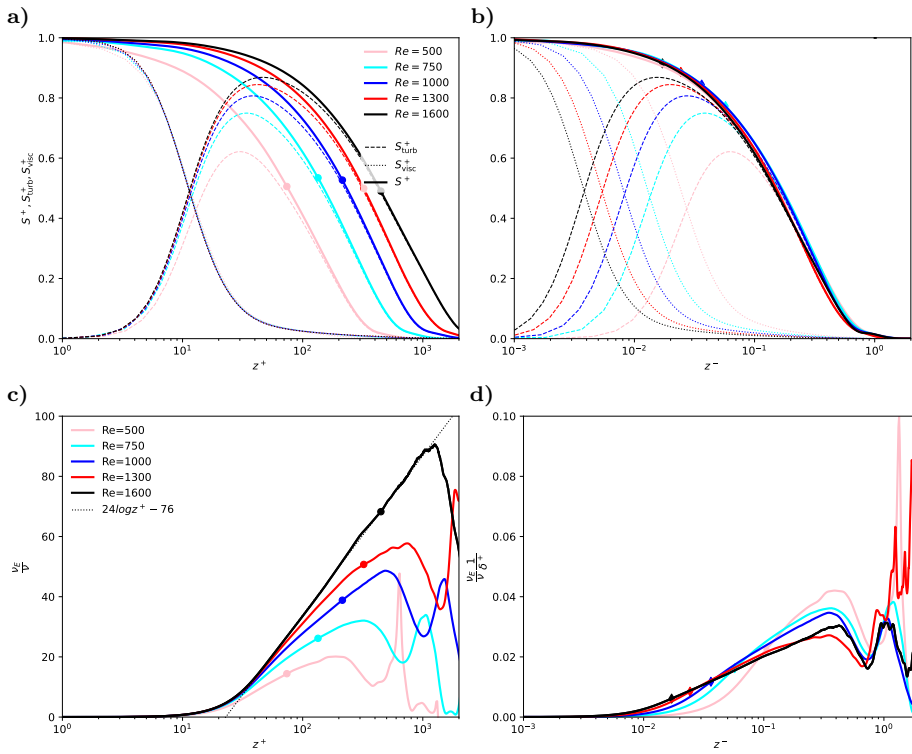


Fig. 2 a-b) Profiles of the turbulent stress S_{turb}^+ (dashed), the viscous stress S_{visc}^+ (dotted), and the total stress, $S^+ = S_{\text{visc}}^+ + S_{\text{turb}}^+$ (solid) as a function of inner height (a) and outer height (b). c-d) Normalized eddy viscosity ν_E (solid) plotted versus inner (c) and outer height (d). Different colors are for different Reynolds numbers (cf. Tab. 1). Circles in (a) and (c) denote the height $z^- = 0.15$, diamonds in (b) and (d) are for $z^+ = 50$ as in Fig. 1.

above, outer scaling is appropriate for the well-established dynamics in the overlap region of inner and outer layer. This, however, implies a mixed scaling for the turbulent stress,

$$S_{\text{turb}} = \sqrt{\overline{uw}^2 + \overline{vw}^2}. \quad (8b)$$

Indeed, S_{turb} only follows inner normalization below $z^+ \lesssim 20$ (where the turbulent contribution is negligible). In the outer layer, where $S_{\text{visc}} \rightarrow 0$, S_{turb}^+ follows outer normalization for $z^- \gtrsim 0.15$ —with increasing accuracy for larger Re and larger distance from the surface. In the overlap region, i.e. for $z^+ > 20$ and $z^- < 0.15$, the mixed scaling for the turbulent stress can be expressed as

$$S_{\text{turb}}^+(z^+, \text{Re}_\tau) = S^+(z^-) - S_{\text{visc}}^+(z^+), \quad (8c)$$

where $z^- = z^+/\text{Re}_\tau$.

The Eddy viscosity plays a crucial part when modelling profiles and the vertical transport in turbulent flow. In analogy to the Fick-law for molecular diffusion, the eddy diffusivity is the effective diffusivity that yields the turbulent transport S_{turb} based on the strain rate. For the symmetries in the flow (horizontal homogeneity, and $W = 0$), it is

$$\nu_E = \frac{S_{\text{turb}}}{\sqrt{\left(\frac{\partial U}{\partial z}\right)^2 + \left(\frac{\partial V}{\partial z}\right)^2}} = \nu \frac{S_{\text{turb}}}{S_{\text{visc}}}. \quad (9a)$$

The inner normalization of ν_E is obtained when dividing by the molecular viscosity:

$$\nu_E^+ = \nu_E/\nu = S_{\text{turb}}/S_{\text{visc}}. \quad (9b)$$

Under this normalization, the profiles of eddy viscosity collapse below $z^+ \approx 20$ with a tendency towards better collapse at higher z^+ for higher Reynolds number (up to $z^+ \approx 50$ for $\text{Re} = 1600$; Fig. 2c). In the outer layer, the eddy viscosity is characterized by a distinct minimum at $z^- \approx 0.6 - 0.8$, and we find that the following mixed normalization of ν_E by the geostrophic wind and friction velocity collapses the value of ν_E at this minimum (cf. Fig. 2d):

$$\nu_E^- = \nu_E^+ \frac{1}{\delta^+} = \nu_E \frac{1}{\nu} \frac{\nu}{u_* \delta} = \nu_E \frac{f}{u_*^2}. \quad (9c)$$

Substantial variation of the profiles is, however observed below and above this minimum for different Re which illustrates that this normalization is probably not generally appropriate across the outer layer.

The organization of the flow is depicted in terms of the turbulence kinetic energy in Fig. 3. In vicinity of the wall, at $y^+ \approx 10$, (Fig. 3a), elongated streaks aligned with the surface shear stress dominate. Moving away from the wall, to $y^+ \approx 150$ (well within the logarithmic region), the structures are larger and more isotropic, but they are still largely aligned with the surface shear stress. In the upper part of the outer layer, around $y^+ \approx 1000$, no clear signature of the surface veering direction is found, and intense TKE structures (bright yellow) are organized on a large spatial scale with weaker eddies (greenish structures) and quiescent regions in between.

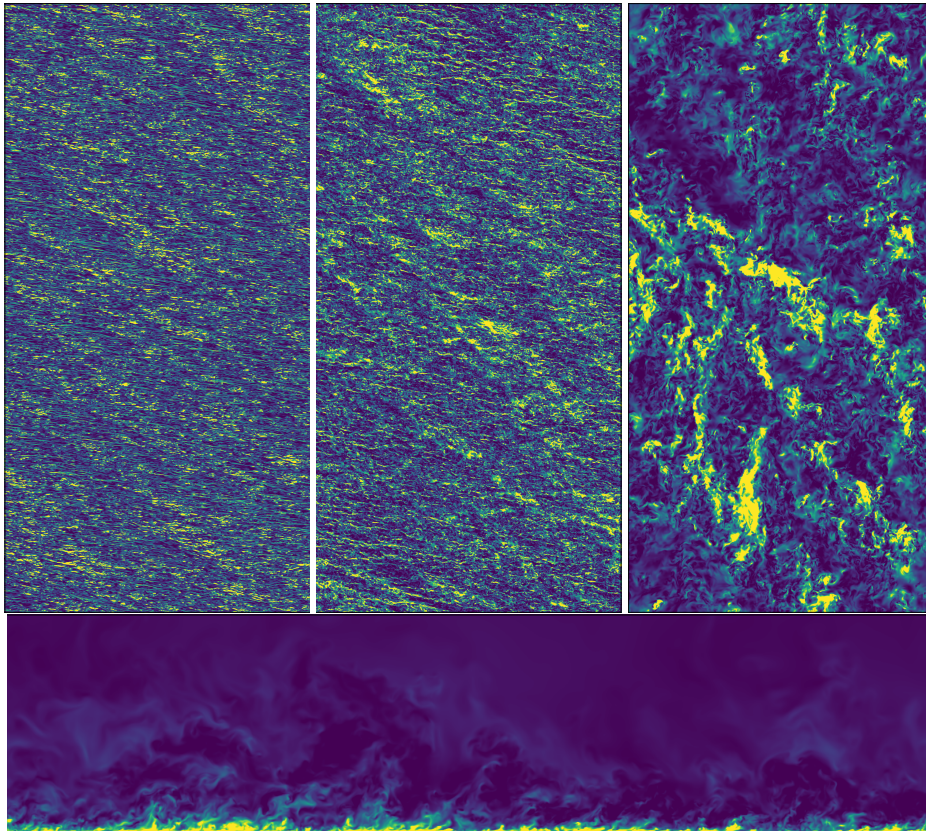


Fig. 3 horizontal slices of turbulence kinetic energy in the Buffer layer ($i=10$), logarithmic Layer ($i=100$), and outer layer ($i=400$); coloring between percentiles 4 and 96 of the respective image. Lower panel:streamwise–vertical intersect through the domain

322 4 A universal velocity profile for the turbulent Ekman layer

323 We now turn to the formulation of a general velocity profile that is fully determined
 324 by the only parameter of the idealized problem, namely a Reynolds number repre-
 325 senting the scale separation or geometric size of the problem. This precludes, first,
 326 a drag law wherewith we begin this section (4.1). Based on the scaling arguments
 327 put forward in Sec. 3, we then develop, second, a formulation of the wind vector
 328 in the Ekman layer (Sec 4.2). Finally, we come up with a separate formulation of
 329 the, third, stream-wise and, fourth, span-wise velocity components in the overlap
 330 and inner regions of the flow.

331 4.1 Drag-Law

332 A drag-law for Ekman flow determines—as a function of Reynolds number alone—
 333 the surface drag. This can be formulated by the normalized surface friction, u_*
 334 (Eq. (1b), also termed geostrophic drag), and the direction of surface shear stress,

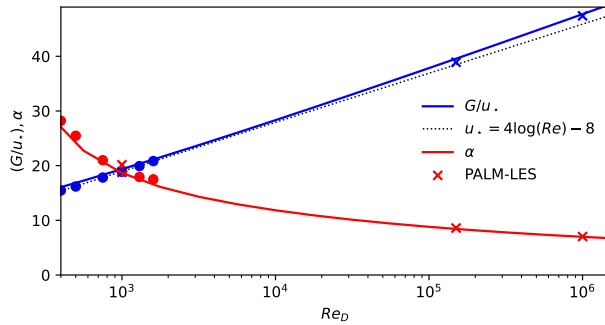


Fig. 4 Variation of geostrophic drag, Z_* , and surface veering, α_* , with Reynolds number according to the theory by Spalart et al. (1989) and as estimated from DNS data

335 α_* (Eq. (1c), also termed wind veer). A non-zero veering of the wind is a rather
 336 special case in comparison with most turbulent flows considered in an engineering
 337 context, and it confronts us with a situation where the most appropriate coordinate
 338 system for analysis (namely that aligned with the surface shear stress) is a priori
 339 unknown. We compare our DNS data against a semi-empirical drag-law based on
 340 integral consideration (Spalart 1989) and find, as demonstrated in previous work
 341 (Ansorge and Mellado 2014), excellent agreement in the range $400 < \text{Re} < 1600$,
 342 representing a factor of 16 in variation of viscosity.

343 We also find that the solution of the transient equation involved in estima-
 344 tion of u_* for a given Reynolds number Re_D is approximated reasonably by the
 345 formulation

$$Z_* = 4 \log(\text{Re}_D) - 8 \quad (10)$$

346 which quantifies the 'weak' dependence of u_* on the Reynolds number as an ap-
 347 proximately logarithmic one, at least for problems with a scale separation on the
 348 order that is relevant to geophysical problems ($Re_D < 10^8$).

349 4.2 Profile in the Ekman layer

350 Formulations for the outer layer that take into account the rotation (and thus
 351 deviation from the channel-flow analogy) need to be matched to the framework of
 352 surface similarity. A smooth transition from the inner layer to the Ekman layer,
 353 where the wind is characterized by a turning of its mean direction, is not eas-
 354 ily achieved. Optis et al. (2014), for instance, define an "effective geostrophic wind
 355 vector that has the same magnitude of the observed surface geostrophic wind and is ro-
 356 tated by the angle α [their nomenclature]" to overcome the unsteady transition when
 357 approaching the Ekman layer from below. Such rotation of the wind vector is *a*
 358 *posteriori* justified by the observational data that the model outcomes are com-
 359 pared to. This need for a connection of the two reference frames is a manifestation
 360 of a mismatch in the theoretical treatment of the inner and outer layer in this
 361 rotating flow configuration.

362 The text-book solution for Ekman flow makes use of the physical boundary
 363 conditions (BCs) for the ABL (no-slip at the bottom and geostrophic wind in the
 364 free atmosphere) and a constant eddy viscosity. Specifying the boundary conditions

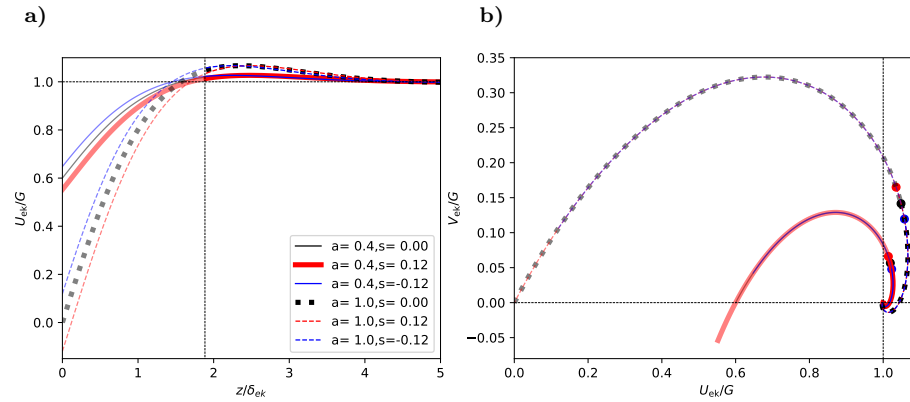


Fig. 5 a) Generalized Ekman-profile of the geostrophic-aligned component U_{ek} . b) Hodograph for the geostrophic-aligned and pressure-gradient aligned components U_{ek} and V_{ek} . Thick, black dashed line shows the classic solution. The height corresponding to $z^- = 0.30$ is marked by the dashed line in panel (a) and by filled circles in panel (b). The hodograph and profiles above this reference height are shown as solid lines, below as opaque line.

365 at top and bottom eliminates one mode of the analytical solution, and it determines
 366 the magnitude of the spiral. In doing so, one has to assume that the solution
 367 is appropriate across the entire ABL, which is not the case: The dynamics put
 368 forth by Ekman in 1905 are not appropriate in the surface layer of the ABL;
 369 better approximations exist for the logarithmic, buffer, and viscous sublayers. In
 370 view of this situation, we use an adapted Ekman spiral that does not enforce the
 371 boundary conditions at the surface but at a different height. This is achieved by
 372 considering the Ekman spiral only in the Ekman layer, thus giving way for the
 373 well-established logarithmic and viscous-layer profiles in the lower surface layer.
 374 Based on the derivation in App. A, this profile is given by

$$\frac{1}{G} \begin{pmatrix} U_{ek} \\ V_{ek} \end{pmatrix} = \begin{pmatrix} 1 \\ 0 \end{pmatrix} + e^{-z_{ek}} \left[a_{ek} \begin{pmatrix} -\cos z_{ek} \\ \sin z_{ek} \end{pmatrix} + b_{ek} \begin{pmatrix} \sin z_{ek} \\ \cos z_{ek} \end{pmatrix} \right]. \quad (11a)$$

375 with $z_{ek} = \delta_{ek}(y^- - s_{ek})$. The right-hand-side consists of two modes with magnitude
 376 a_{ek} and b_{ek} shifted by $\pi/2$ with respect to each other. In the classic case, the second
 377 mode governed by b_{ek} is incompatible with the surface boundary condition. While
 378 this is not the case here for the general form of the profile, the phase shifts can also
 379 be captured by the parameter s_{ek} , and we stick with to a single-modal approach,
 380 i.e., we let $b_{ek} = 0$.

381 This single-modal solution is characterized by three parameters, (i) an Ekman-
 382 layer depth scale δ_{ek} , (ii) the magnitude parameter of the spiral a_{ek} , and (iii) a
 383 zero-crossing point for the velocity s_{ek} . The effects of varying these parameters
 384 are illustrated in Fig. 5 where the classic Ekman solution is recovered by setting
 385 $a_{ek} = 1$, $s_{ek} = 0$ and $\delta_{ek} = \sqrt{2\nu/f}$. These parameters are *a priori* unknown as
 386 they need to conform to the turbulent state of the boundary layer; we use our
 387 DNS data to arrive at best estimates for them.

388 **The Ekman-layer depth scale** δ_{ek} is fundamentally defined by the eddy vis-
 389 cosity. However, we have seen in Section 3 that a characteristic value for the eddy
 390 diffusivity is not easily obtained for its strong dependence on the Reynolds number

and distance from the surface. We therefore resort to the physical manifestation of the eddy diffusivity in an Ekman layer, and use the boundary layer depth $\delta_{\text{ek}} = 0.66\delta \times 2\pi$. For the relation $\delta_{\text{ek}} = \sqrt{2\nu_{\text{ek}}/f}$, this yields $\nu_{\text{ek}} \propto u_*^2/f$ in accordance with the observations in Sec. 3 (Eq. 9c).

The magnitude parameter of the Ekman spiral, a_{ek} , defines the super-geostrophic maximum of the wind profile aloft the logarithmic layer. Our simulations suggest this maximum of the velocity deficit remains constant when normalized by u_* as shown in Fig. 6. The numerical value of a_{ek} is estimated from visual comparison, and we find $a_{\text{ek}} = 8.4u_*$; while this appears rather large, it is pre-multiplied by $e^{-z_{\text{ek}}}$ which has already decreased to $\mathcal{O}(0.1)$ at the height of this maximum. This choice ascertains that the velocity deficits $U/u_* - Z_*$ and $V/u_* - Z_*$ do not depend on the velocity scale u_* , but only on G as

$$U_{\text{ek}}/u_* - Z_* \propto a_{\text{ek}}Z_* = 8.4G. \quad (12)$$

Thus, the reduction of the area under the Ekman hodograph is directly linked to the variation in the friction velocity, which quantifies the well-known qualitative observation that a more turbulent boundary layer leads to a flatter hodograph in Ekman flow.

The offset parameter s_{ek} defines the zero-crossing height of the profile (in contrast to δ_{ek} , which determines the thickness across which the wind veering takes place). Physically, this offset can be understood as the height at which the surface was located assuming a perfect Ekman flow down to the surface. As this is not the case, and gradients are steeper in the highly turbulent boundary layer flow encountered when approaching the surface, the offset is smaller than zero (the fully turbulent boundary layer is actually thinner than an Ekman layer would be). From our DNS data, we estimate $s_{\text{ek}} = -0.12$.

In summary, the outer layer of Ekman flow is characterized by a turning of the wind velocity and the super-geostrophic maximum that is sustained by momentum convergence at the inflection point of the velocity profile. The super-geostrophic maximum of streamwise velocity and a secondary minimum aloft the bulk-turbulent part of the boundary layer are well-described by a classic Ekman spiral with adapted boundary conditions and a shift in reference height. Corresponding profiles are shown in comparison with data from three DNS runs in Fig. 6. The idealized profiles capture the secondary minimum and convergence to the geostrophic equilibrium in the non-turbulent flow very well.

4.3 Streamwise Velocity Component

For the streamwise velocity profile (that in non-rotating flows due to the geometry is always aligned with the surface shear stress), well-established theories exist for various regimes according to their distance from the wall and the relative role of viscosity, turbulence and interaction with the outer region of the flow with the logarithmic law for the mean velocity as a central anchor point.

In immediate vicinity to the surface, local turbulent mixing cannot occur for the no-slip/no-penetration boundary condition, and the mean velocity is described by a viscous profile of the form

$$U^{\alpha_*+} = z^+ \quad (13a)$$

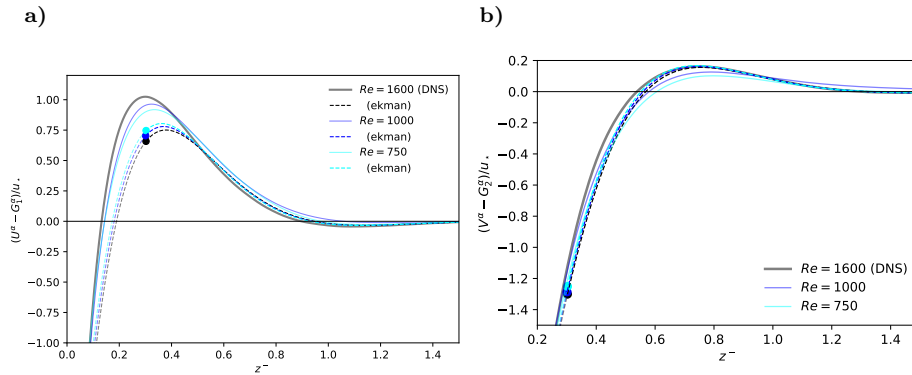


Fig. 6 Shear-aligned velocity deficit for the wall-streamwise (panel (a)) and wall-spanwise (panel (b)) components of the mean velocity U^{α} and V^{α} . Solid lines show DNS data, dashed lines the Ekman profiles U_{ek} and V_{ek} as defined in Eq. 11. Region below $z^- = 0.3$ is shown opaque. Variations in U_{ek} and V_{ek} are a consequence of the normalization and related to changes in u_* and α_* among the different Re_D .

433 where the direction of the velocity points into the exact opposite direction of the
 434 wall shear stress τ . In absence of roughness elements and for small roughness
 435 ($z_0^+ < 5$), this linear regime is known as viscous sub-layer Foken (2002); Foken
 436 et al. (1978). In fact, this law of the wall has no degree of freedom given the
 437 drag, i.e. once u_* and α_* are defined. However, theoretical foundation is lacking
 438 for the exact shape of the velocity profile in the buffer layer; though crucial for
 439 turbulence production, it is commonly understood as a transition region between
 440 the linear profile at the surface and the logarithmic profile aloft. A pure blending
 441 from the linear velocity profile into the logarithmic one is, however, not reasonable
 442 as both the linear and logarithmic profile overestimate the velocity in the buffer
 443 layer. We therefore introduce a two-step correction procedure, accounting for the
 444 smaller-than linear growth beyond $y^+ \approx 5$, and assuring smooth matching with
 445 the logarithmic law at $y^+ = 40$:

$$U_{\text{inner}}^{\alpha_* +} = \frac{z^+}{1 + c_1(y^+)^2} + (c_2 y^+ - a_{\text{match}}) \frac{1 + \tanh[0.2(y^+ - 22)]}{2} + c_3 e^{-c_4(y^+ - 22)^2}. \quad (13b)$$

446 We use here

$$c_1 = 0.00185; \quad c_2 = 0.195; \quad c_3 = 0.4; \quad c_4 = 0.35.$$

447 The second and third terms on the right hand side vanish for $y^+ \ll 22$, and
 448 $c_1 = 0.00185$ implies an approximately 5% correction at $y^+ = 5$ and an 18.5%
 449 correction at $y^+ = 10$. The second and third term on the R.H.S. of eq. (13b) are
 450 an empirical fit to the velocity profiles observed in the buffer layer and appear
 451 independent of the Reynolds number for the range observed here. The coefficient
 452 a_{match} , which has no effect in the viscous sublayer, is then used to match this
 453 formulation to the logarithmic law employed above.

454 In the logarithmic region, we use the profile

$$U_{\log}^{\alpha_* +} = \frac{1}{\kappa} \log y^+ + C \quad (13c)$$

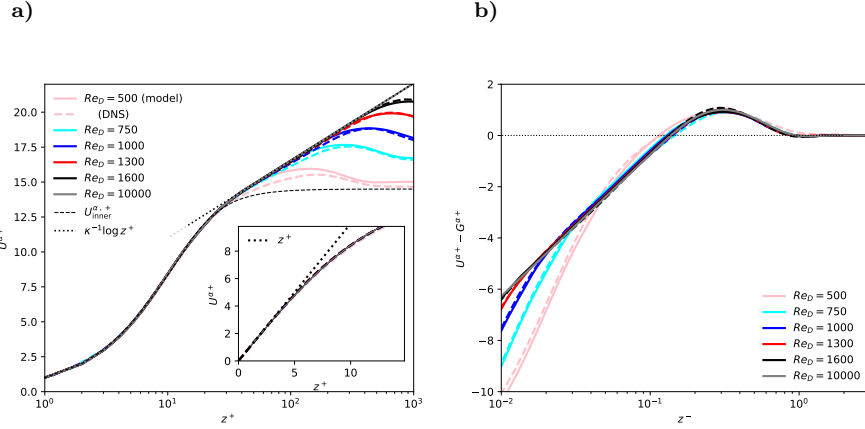


Fig. 7 Shear-aligned profiles of velocity components $U^{\alpha*+}$ in inner (left) and outer (right) units.

455 with the von-Kármán constant $\kappa = 0.416$ and the boundary condition $C = 5.4605$.
456 For this logarithmic law, $a_{\text{match}} = 3.569861$ for a matching at $y^+ = 40$.

457 4.4 Spanwise velocity component

458 The background rotation and associated veering of the surface wind implies a
459 non-zero profile for the span-wise velocity which challenges the conventional as-
460 sumptions related to the channel-flow analogy: While the analogy with channel
461 flow in vicinity of the wall implies that the streamwise component be zero or at
462 least small, the veering requires a value of $V_{top} = U_G \sin \alpha_*$ in the free stream (and
463 thus also at the top of the boundary layer if we assume that any substantial veloc-
464 ity gradient is confined to the turbulent part of the flow). This continuous rotation
465 of the wind vector is conveniently visualized by velocity hodographs aligned with
466 the outer, geostrophic flow (cf. Fig. 5b) and normalized by the geostrophic wind.
467 The geometry of the flow and its drag imply the following for any hodograph: (i)
468 the boundary conditions at the surface, (ii) the boundary condition at the top,
469 and (iii) the inclination of the hodograph at the origin by the surface veering:

$$V^{\alpha*}(z=0) = 0, \quad (14a)$$

$$\lim_{z \rightarrow \infty} V^{\alpha*} = G \sin \alpha_* \quad (14b)$$

$$\partial_{z^+} V^{\alpha*+}|_{z=0} = 0. \quad (14c)$$

470 Outer scaling of the velocity profile further implies that the velocity deficit of
471 $(V^{\alpha*} - G^{\alpha*})/u_*$ be a universal function of the outer height z^- . In the outer region
472 of the flow (for $z^- \rightarrow 1$), $f_V(z^-)$, should govern the spanwise velocity profile, as
473 is supported by our DNS data (Fig. 1b); above $z^- \approx 0.3$, this profile is very well
474 approximated by the Ekman-turning derived above (Eq. (11); Fig. 6b). While this
475 deficit is a signature of outer rotation, it is inappropriate to extend this general
476 relation to the surface where inner scales matter: On the one hand, the variation
477 of the spanwise velocity deficit across the boundary layer (i.e. between $0 < z^- < 1$)

478 must match the difference implied by the drag law (u_* , α_*) and the constant value
 479 of V^{α_*} around $z^- = 0.3$. On the other hand,—provided the outer velocity deficit
 480 is Re independent—the Re-dependence of α_* and u_* implies that this difference
 481 cannot be constant as a function of Re

482 We hence ask, how does the span-wise component scale when the surface is
 483 approached? Clearly, the spanwise contribution is small in comparison with the
 484 streamwise component throughout much of the layer below $z^- \approx 0.3$. However, we
 485 cannot assume $V = 0$ if a smooth matching between the inner and outer layers shall
 486 be achieved. In this context, we first realize that the velocity deficit $(V^{\alpha_*} - G^{\alpha_*})/u_*$
 487 approaches a Re-independent constant around $C_{V0} = Z_* \sin \alpha = 6.1$ at the surface;
 488 deviations from this constant are only found for the lowest Reynolds numbers
 489 which is in accordance with the low-Re correction suggested by Spalart (1989).
 490 This constrains the wind veer, and it quantitatively shows that the decreasing
 491 wall friction manifest in an increase of Z_* exactly compensates the decrease of
 492 wind turning measured by $\sin \alpha_*$.

493 If the difference across the boundary layer is constant (C_{V0}) vs. Re, the av-
 494 eraged gradient $\partial_{z+} V^{\alpha_*+}$ of the spanwise velocity component must decrease as
 495 $1/\delta^+$ with increasing Re_τ . Hence, it should—at a fixed height—be $V^{\alpha_*} \propto (\delta^+)^{-1}$. A
 496 profile that agrees with the constraints of the profile at the surface and exploits
 497 the dependence of V^{α_*} on δ^+ is

$$V^{\alpha_*} \frac{\delta^+}{G} = f_{V,\text{visc}}(z^+) = v_{\text{ref}} (\omega_v z^+ - 1 + \exp[-\omega_v z^+]), \quad (15)$$

498 where v_{ref} controls the magnitude of the profile and ω_v sets the height at which the
 499 profile transitions into an approximately linear one. We find excellent agreement
 500 with the DNS data for $500 \leq Re_D \leq 1600$ below $z^+ \approx 15$ with

$$v_{\text{ref}} = 18.85; \quad \omega_v = 0.2353$$

501 (cf. Fig. 8b).

502 For the adjacent surface layer, we find a log-like transition from the quasi-linear
 503 profile inner profile around $z^+ = 10$ to a linear profile with increasing Re (Fig. 8b).
 504 We model this transition by

$$f_{V,\log}(z^+) = \frac{V_{\log}(z^+)}{G} \delta^+ = a_{\log} + b_{\log} \log z^+ + c_{\log} z^+. \quad (16)$$

505 This surface-layer profile matches the inner (viscous) scaling in vicinity of the
 506 surface to the outer (Ekman) scaling above $z^- = 0.3$ when constrained by the
 507 viscous profile at the bottom and the Ekman profile at the top:

$$f_{V,\log}(z^+ = 10) = \quad f_{V,\text{visc}}(z^+ = 10) =: \quad v_{10} \simeq 27.3 \quad (17)$$

$$\frac{\partial}{\partial z^+} [f_{V,\log}]_{z^+ = 10} = \quad \frac{\partial}{\partial z^+} [f_{V,\text{visc}}]_{z^+ = 10} =: \quad d_{10} \simeq 4.01 \quad (18)$$

$$f_{V,\log}(z^+ = 0.3\delta^+) = \quad V_{\text{ek}}^{\alpha_*}(z^- = 0.3)\delta^+ =: \quad v_{03} \quad (19)$$

508 where v_{03} is determined by $V_{\text{ek}}(0.3)$ and $U_{\text{ek}}(0.3)$ and depends on Re. Given the
 509 Ekman formulation of the velocity profile introduced in Sec. 4.2, one may express
 510 v_{03} using the Ekman profile introduced in Sec. 4.2 together with the approximation
 511 for $u_*(Re)$ found in Eq. (10). While the Re-dependency of a_{\log} , b_{\log} , c_{\log} is small,

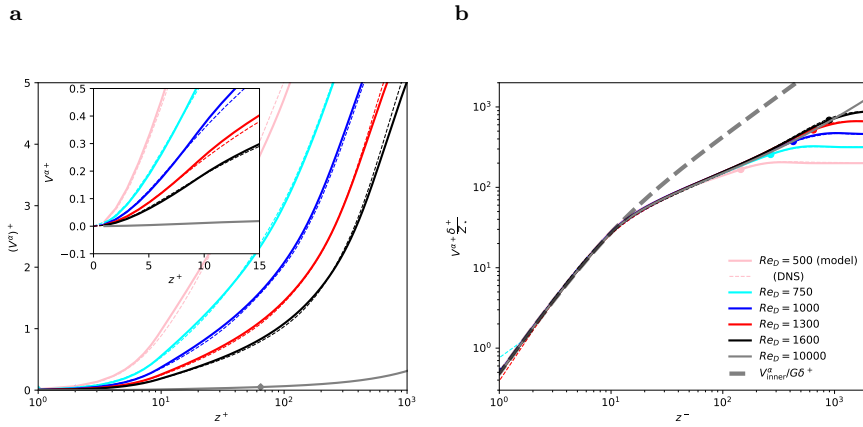


Fig. 8 Profiles of shear-aligned span-wise velocity $(W^\alpha)^+$ versus inner height. Dashed lines show DNS data, thick, opaque lines are from the semi-empirical theory developed above. Left panel show standard inner normalization. Right panel shows the inviscid normalization yielding a universal profile for the spanwise component of velocity in the inner layer.

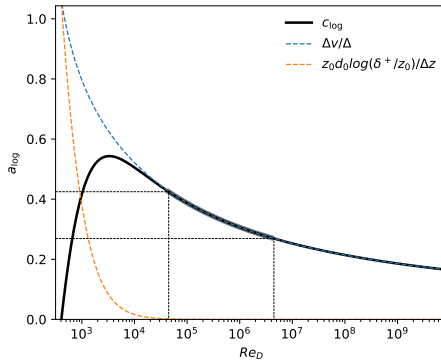


Fig. 9 Coefficients a_{\log} , b_{\log} and c_{\log} (cf. Eq. 16) as a function of the viscous Reynolds number Re_D . The approximate range of scale separation relevant for atmospheric application is found in between the dotted lines, where $a_{\log} \simeq 0$ and $c_{\log} \simeq 0.4$

512 it shows up in Fig. 1 where the normalized profiles of spanwise velocity become
 513 more convex with increasing Re . We can now quantify this effect by means of the
 514 change of c_{\log} versus Re which is shown in Fig. 9 (cf. Appendix B; a_{\log} and b_{\log}
 515 are then determined by the universal values of v_{10} and d_{10}).

516 5 Discussion

517 5.1 Implications for surface-layer scaling

518 Eq. (15) establishes a universal mixed scaling for the spanwise velocity in the vis-
 519 ous layer: While it requires the vertical coordinate to be expressed in inner units,
 520 the velocity itself is normalized by the geostrophic wind, and becomes inversely

proportional to the friction Reynolds number $\text{Re}_\tau = \delta^+$ when considered at a fixed height. In vicinity of the surface, such mixed scaling has already been identified for higher-order statistics in convective flows (Mellado et al. 2016; Li et al. 2018), where large scales leave their signatures in vicinity of the surface. It is important to note here that, while V is a first-order statistic from a statistical perspective, the spanwise velocity is a higher-order correction term from the perspective of similarity theory and from the viewpoint of the channel-flow analogy that is routinely employed in the surface layer. Further, this is consistent with the scaling for the velocity hodograph found in Eq. (12) where the friction velocity also drops out.

In the surface layer, there is not only a mixed scaling—as we had already identified in the viscous layer—, but we cannot find a universal function onto which the profiles of spanwise velocity collapse. This additional degree of freedom reflects the inner–outer matching problem for the spanwise velocity, and rather than giving a universal profile for this region, as is usually done, we resort here to a parametric description of the problem, namely in terms of the function $f_{V,\log}$ determined by the parameters a_{\log} , b_{\log} , c_{\log} which can be estimated based on the above scaling considerations for any Reynolds number. We note that, once the parameter a_{\log} is known, the parameters b_{\log} and c_{\log} can be estimated solely based on $f_{V,\text{visc}}$, i.e. using the value v_{10} and d_{10} found for the viscous region of the flow. For the range of Reynolds number relevant to geophysical problems ($10^4 \lesssim \text{Re}_D \lesssim 10^6$), the variation of c_{\log} is, however, rather small.

5.2 Comparison with other theories

An alternative approach that considers viscous effects close to the surface is the van-Driest scaling (Van Driest 1956), where an exponential damping of Prandtl's mixing length is considered near the wall to yield

$$\frac{\partial u^+}{\partial y^+} = \frac{2}{1 + \sqrt{1 + (2\kappa y^+)^2 (1 - \exp[-y^+])}}; \quad (20)$$

the spanwise component is zero as no rotational effects are considered. Comparing our proposed formulation for the stream-wise velocity in the inner layer to Van Driest's formulation yields later convergence of the velocity onto the logarithmic profile while, over all, it serves as an excellent model of the streamwise velocity component: Notable deviations (on the order of few percent) only occur in the region $10 < z^+ < 30$, where the velocity transitions from the linear to the logarithmic profile.

Compare to Emeis (2002) and Gryning (2007); highlight explicit knowledge on veering-profile → directional sheer;

Remember of interpretation in the context of eddy viscosity (Fig. 2) Consider Townsend “Turbulent Shear Flow” Chapter 7.18: p. 319

Implications for **K-theory** (we now can consider that shear and stress are not necessarily perfectly aligned). → can we do something to infer a K-profile from these theoretical considerations?

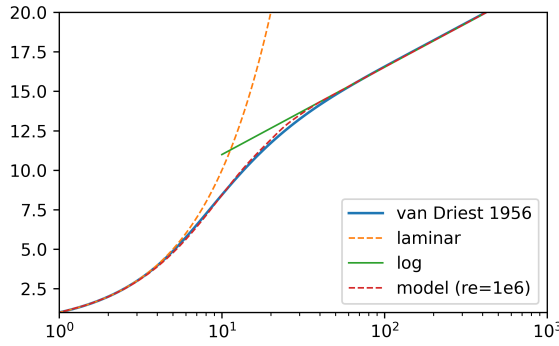


Fig. 10 Near-wall velocity profile according to the van-Driest scaling (blue, solid) in comparison with the present model (red, dashed), the viscous law of the wall (orange dashed), and the logarithmic law (green, solid)

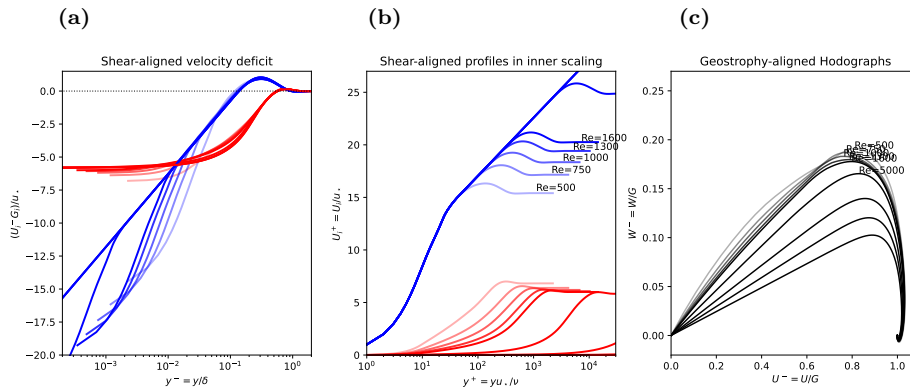


Fig. 11 (a) Velocity deficit, (b) velocity profile in shear-aligned hodographs and (c) hodograph in geostrophy-aligned coordinates. Thick, solid lines show theory, dashed lines data from DNS.

560 6 Conclusions

561 Applications:

- 562 – reference-shear for neutral profile approaches(systematic!) → wind engineering!
- 563 – initial condition for LES/DNS to eliminate/minimize inertial oscillation in
- 564 Benchmark simulations
- 565 –

566 References

- 567 Ansorge C (2019) Scale Dependence of Atmosphere–Surface Coupling Through
568 Similarity Theory. Boundary-Layer Meteorol 170(1):1–27, DOI 10.1007/
569 s10546-018-0386-y
- 570 Ansorge C (2024a) Direct numerical simulation of turbulent Ekman flow
571 (Re=0500): DOI 10.17169/refubium-42505. DOI 10.17169/refubium-42505

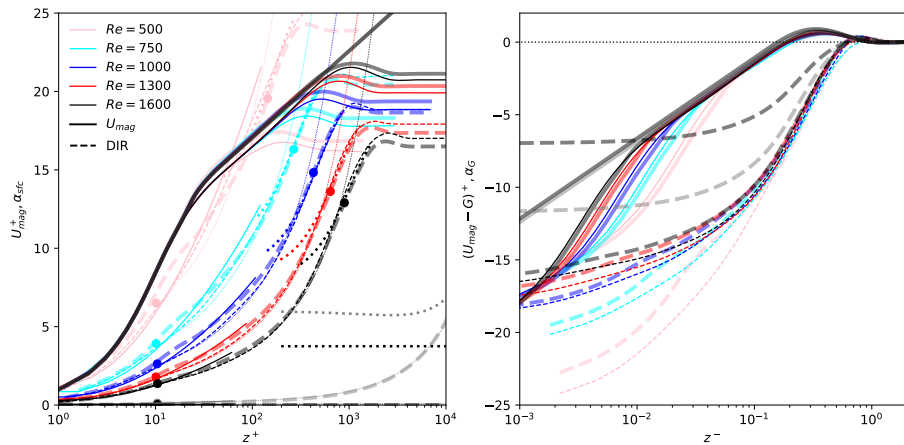


Fig. 12 Total velocity and veering (in degrees) vs inner and outer height. Dashed lines show DNS data, thick lines are from semi-empirical theory.

- 572 Ansorge C (2024b) Direct numerical simulation of turbulent Ekman flow
573 ($Re=1000$): DOI 10.17169/refubium-42507. DOI 10.17169/refubium-42507
574 Ansorge C (2024c) Direct numerical simulation of turbulent Ekman flow
575 ($Re=1300$): DOI 10.17169/refubium-42508. DOI 10.17169/refubium-42508
576 Ansorge C (2024d) Direct numerical simulation of turbulent Ekman flow
577 ($Re=1600$): DOI 10.17169/refubium-42509. DOI 10.17169/refubium-42509
578 Ansorge C, Mellado JP (2014) Global Intermittency and Collapsing Turbulence in
579 the Stratified Planetary Boundary Layer. *Boundary-Layer Meteorol* 153(1):89–
580 116, DOI 10.1007/s10546-014-9941-3
581 Ansorge C, Mellado JP (2016) Analyses of external and global intermittency in
582 the logarithmic layer of Ekman flow. *J Fluid Mech* 805:611–635, DOI 10.1017/
583 jfm.2016.534
584 Baars WJ, Marusic I (2020) Data-driven decomposition of the streamwise turbu-
585 lence kinetic energy in boundary layers. Part 2. Integrated energy and. *J Fluid*
586 *Mech* 882:A26, DOI 10.1017/jfm.2019.835
587 Barenblatt GI (1993) Scaling laws for fully developed turbulent shear flows. Part
588 1. Basic hypotheses and analysis. *J Fluid Mech* 248:513–520, DOI 10.1017/
589 S0022112093000874
590 Barenblatt GI, Goldenfeld N (1995) Does fully developed turbulence exist?
591 Reynolds number independence versus asymptotic covariance. *Phys Fluids*
592 7(12):3078–3082, DOI 10/bw2sqz
593 Blackadar AK, Tennekes H (1968) Asymptotic Similarity in Neutral Barotropic
594 Planetary Boundary Layers. *Journal of the Atmospheric Sciences* 25:1015–1020,
595 DOI 10.1175/1520-0469(1968)025<1015:ASINBP>2.0.CO;2
596 Brown AR, Beljaars ACM, Hersbach H, Hollingsworth A, Miller M, Vasiljevic
597 D (2005) Wind turning across the marine atmospheric boundary layer. *Quar-
598 terly Journal of the Royal Meteorological Society* 131(607):1233–1250, DOI
599 10/dw2bxz
600 Calaf M, Meneveau C, Meyers J (2010) Large eddy simulation study of fully de-
601 veloped wind-turbine array boundary layers. *Phys Fluids* 22(1):015,110, DOI

- 602 10/b7gc6v
603 Coleman GN, Ferziger JH, Spalart PR (1992) Direct Simulation of the Stably
604 Stratified Turbulent Ekman Layer. *Journal of Fluid Mechanics* 244:677–712,
605 DOI 10.1017/S0022112092003264
606 da Silva CB, Hunt JC, Eames I, Westerweel J (2014) Interfacial Layers Between
607 Regions of Different Turbulence Intensity. *Annu Rev Fluid Mech* 46(1):567–590,
608 DOI 10.1146/annurev-fluid-010313-141357
609 Dimotakis PE (2005) TURBULENT MIXING. *Annual Review of Fluid Mechanics*
610 37(1):329–356, DOI 10.1146/annurev.fluid.36.050802.122015
611 Ekman VW (1905) On the influence of the earth's rotation on ocean currents. *Ark
612 Mat Astron Fys*, Vol 2 (1905), pp 1-53 2:1–53
613 Ellison TH (1955) The Ekman spiral. *Q J Roy Met Soc* 81(350):637–638, DOI
614 10.1002/qj.49708135025
615 Emeis S (2018) Wind Energy Meteorology, 2nd edn. *Atmospheric Physics for Wind
616 Power Generation*, Springer, Heidelberg
617 Emeis S, Baumann-Stanzer K, Piringer M, Kallistratova M, Kouznetsov R,
618 Yushkov V (2007) Wind and turbulence in the urban boundary layer analysis
619 from acoustic remote sensing data and fit to analytical relations. *metz* 16(4):393–
620 406, DOI 10.1127/0941-2948/2007/0217
621 Esau I (2004) Simulation of Ekman Boundary Layers by Large Eddy Model with
622 Dynamic Mixed Subfilter Closure. *Environmental Fluid Mechanics* 4(3):273–
623 303, DOI 10/b8f3kh
624 Etling D (2002) Theoretische Meteorologie, 2nd edn. *Eine Einführung*, Springer-
625 Verlag, Berlin, Heidelberg
626 Foken T (2002) Some aspects of the viscous sublayer. *metz* 11(4):267–272, DOI
627 10.1127/0941-2948/2002/0011-0267
628 Foken Th, Kitajgorodskij SA, Kuznecov OA (1978) On the dynamics of the
629 molecular temperature boundary layer above the sea. *Boundary-Layer Meteorol*
630 15(3):289–300, DOI 10.1007/BF02652602
631 Ghannam K, Bou-Zeid E (2021) Baroclinicity and directional shear explain departures
632 from the logarithmic wind profile. *Quarterly Journal of the Royal Meteorological Society*
633 147:434–464, DOI 10/gnj6z2
634 Gryning SE, Batchvarova E, Brümmer B, Jørgensen H, Larsen S (2007) On
635 the extension of the wind profile over homogeneous terrain beyond the sur-
636 face boundary layer. *Boundary-Layer Meteorol* 124(2):251–268, DOI 10.1007/
637 s10546-007-9166-9
638 Högström U (1988) Non-dimensional wind and temperature profiles in the atmo-
639 spheric surface layer: A re-evaluation. *Boundary-Layer Meteorology* 42:55–78,
640 DOI 10.1007/BF00119875
641 Högström U (1996) Review of some basic characteristics of the atmospheric surface
642 layer. *Boundary-Layer Meteorology* 78(3-4):215–246, DOI 10.1007/BF00120937
643 Jacobs AF, Van Boxel JH (1988) Changes of the displacement height and rough-
644 ness length of maize during a growing season. *Agricultural Forest Meteorol*
645 42(1):53–62, DOI 10.1016/0168-1923(88)90066-4
646 Jiang Q, Wang S, Sullivan P (2018) Large-Eddy Simulation Study of Log Laws
647 in a Neutral Ekman Boundary Layer. *Journal of the Atmospheric Sciences*
648 75(6):1873–1889, DOI 10.1175/JAS-D-17-0153.1
649 Jiménez J (2012) Cascades in Wall-Bounded Turbulence. *Ann Rev Fluid Mech*
650 44(Volume 44, 2012):27–45, DOI 10.1146/annurev-fluid-120710-101039

- 651 Kelly M, Gryning SE (2010) Long-Term Mean Wind Profiles Based on
652 Similarity Theory. *Boundary-Layer Meteorol* 136(3):377–390, DOI 10.1007/
653 s10546-010-9509-9
- 654 Kelly M, Troen I (2016) Probabilistic stability and ‘tall’ wind profiles: Theory
655 and method for use in wind resource assessment. *Wind Energy* 19(2):227–241,
656 DOI 10.1002/we.1829
- 657 Klein M, Maier RE, Schmidt H (2021) Stochastic modeling of transient neutral
658 and stably-stratified Ekman boundary layers. *P A M M* 21(1):e202100,146, DOI
659 10.1002/pamm.202100146
- 660 Li Q, Gentine P, Mellado JP, McColl KA (2018) Implications of Nonlocal Trans-
661 port and Conditionally Averaged Statistics on Monin–Obukhov Similarity The-
662 ory and Townsend’s Attached Eddy Hypothesis. *J Atmos Sci* 75(10):3403–3431,
663 DOI 10.1175/JAS-D-17-0301.1
- 664 Lindvall J, Svensson G (2019) Wind turning in the atmospheric boundary layer
665 over land. *Q J Roy Met Soc* 145(724):3074–3088, DOI 10.1002/qj.3605
- 666 Marusic I, Monty JP, Hultmark M, Smits AJ (2013) On the logarithmic region in
667 wall turbulence. *J Fluid Mech* 716:R3, DOI 10.1017/jfm.2012.511
- 668 Mellado J, Ansorge C (2012) Factorization of the Fourier transform of the pressure-
669 Poisson equation using finite differences in colocated grids. *Z angew Math Mech*
670 92(5):380–392, DOI 10.1002/zamm.201100078
- 671 Mellado JP, van Heerwaarden CC, Garcia JR (2016) Near-Surface Effects of
672 Free Atmosphere Stratification in Free Convection. *Boundary-Layer Meteorol*
673 159(1):69–95, DOI 10.1007/s10546-015-0105-x
- 674 Mirocha JD, Churchfield MJ, Muñoz-Esparza D, Rai RK, Feng Y, Kosović B,
675 Haupt SE, Brown B, Ennis BL, Draxl C, Sanz Rodrigo J, Shaw WJ, Berg LK,
676 Moriarty PJ, Linn RR, Kotamarthi VR, Balakrishnan R, Cline JW, Robin-
677 son MC, Ananthan S (2018) Large-eddy simulation sensitivities to variations of
678 configuration and forcing parameters in canonical boundary-layer flows for wind
679 energy applications. *Wind Energy Science* 3(2):589–613, DOI 10/gn3nh4
- 680 Moin P, Mahesh K (1998) Direct numerical simulation: A tool in turbulence re-
681 search. *Annual Review of Fluid Mechanics* 30:539–578, DOI 10.1146/annurev.
682 fluid.30.1.539
- 683 Momen M, Bou-Zeid E (2016) Large-Eddy Simulations and Damped-Oscillator
684 Models of the Unsteady Ekman Boundary Layer*. *Journal of the Atmospheric
685 Sciences* 73(1):25–40, DOI 10.1175/JAS-D-15-0038.1
- 686 Momen M, Bou-Zeid E, Parlange MB, Giometto M (2018) Modulation of Mean
687 Wind and Turbulence in the Atmospheric Boundary Layer by Baroclinicity.
688 *Journal of the Atmospheric Sciences* 75(11):3797–3821, DOI 10/gfmn67
- 689 Monin AS (1970) The Atmospheric Boundary Layer. *Annual Review of Fluid
690 Mechanics* 2:225–250, DOI 10.1146/annurev.fl.02.010170.001301
- 691 Monin AS, Yaglom AM (1975) Statistical Fluid Mechanics, Vol. II, Dover Publi-
692 cations on Physics, vol II. Dover Publications, Inc., Mineola
- 693 Optis M, Monahan A, Bosveld FC (2014) Moving Beyond Monin-Obukhov Similar-
694 ity Theory in Modelling Wind-Speed Profiles in the Lower Atmospheric Bound-
695 ary Layer under Stable Stratification. *Boundary-Layer Meteorology* 153(3):497–
696 514, DOI 10.1007/s10546-014-9953-z
- 697 Rossby CG, Montgomery RB (1935) The layer of frictional influence in wind and
698 ocean currents. *Papers in Physical Oceanography and Meteorology* III(3):1–101

- 699 Sakagami Y, Haas R, Passos JC (2020) Generalized Non-dimensional Wind
 700 and Temperature Gradients in the Surface Layer. *Boundary-Layer Meteorol*
 701 175(3):441–451, DOI 10.1007/s10546-020-00510-3
- 702 Spalart PR (1989) Theoretical and numerical study of a three-dimensional turbu-
 703 lent boundary layer. *J Fluid Mech* 205(-1):319, DOI 10.1017/S0022112089002053
- 704 Spalart PR, Coleman GN, Johnstone R (2008) Direct numerical simulation of the
 705 Ekman layer: A step in Reynolds number, and cautious support for a log law
 706 with a shifted origin. *Phys Fluids* 20(10):101,507, DOI 10.1063/1.3005858
- 707 Spalart PR, Coleman GN, Johnstone R (2009) Retraction: “Direct numerical sim-
 708 ulation of the Ekman layer: A step in Reynolds number, and cautious support
 709 for a log law with a shifted origin” [Phys. Fluids 20, 101507 (2008)]. *Phys Fluids*
 710 21(10):109,901, DOI 10.1063/1.3247176
- 711 Stoll R, Gibbs JA, Salesky ST, Anderson W, Calaf M (2020) Large-Eddy Sim-
 712 ulation of the Atmospheric Boundary Layer. *Boundary-Layer Meteorol* 177(2-
 713 3):541–581, DOI 10/gmbmzw
- 714 Svensson G, Holtslag AAM (2009) Analysis of Model Results for the Turning
 715 of the Wind and Related Momentum Fluxes in the Stable Boundary Layer.
 716 *Boundary-Layer Meteorol* 132(2):261–277, DOI 10/bwknmt
- 717 Tennekes H (1973) A Model for the Dynamics of the Inversion Above a Convective
 718 Boundary Layer. *Journal of the Atmospheric Sciences*
- 719 Van Driest ER (1956) On Turbulent Flow Near a Wall. *Journal of the Aeronautical
 720 Sciences* 23(11):1007–1011, DOI 10.2514/8.3713
- 721 Zikanov O, Slinn DN, Dhanak MR (2003) Large-eddy simulations of the wind-
 722 induced turbulent Ekman layer. *J Fluid Mech* 495:343–368, DOI 10/ccpbw

723 **A Laminar Ekman solution with consideration of inner layer**

$$\begin{pmatrix} \partial_t U \\ \partial_t W \end{pmatrix} = \begin{pmatrix} fW & + \nu \partial_z^2 U \\ -f(U - G) + \nu \partial_z^2 W \end{pmatrix} \quad (21a)$$

$$\Rightarrow \partial_t(U + iW) = f(W - i(U - G)) + \nu \partial_z^2(U + iW) \quad (21b)$$

724 In stationary conditions, this system is solved by

$$\hat{u}(z) = U_\infty + e^{-\gamma z} [A \cos \gamma z + B \sin \gamma z] \quad (21c)$$

$$\hat{w}(z) = W_\infty + e^{-\gamma z} [-A \sin \gamma z + B \cos \gamma z] \quad (21d)$$

725 where the constants U_∞ , W_∞ set the top boundary condition and A and B set the bottom
 726 boundary condition. The most common boundary condition for a surface Ekman layer is $A =$
 727 $U_\infty = G$, $B = 0$, and $W_\infty = 0$. The lower boundary condition, however, neglects the existence
 728 of the surface layer, and it appears reasonable to define $A = cG$ where $c < 1$ is a constant
 729 that incorporates the increased shear in the surface layer. Given a ‘matching height’ z_{match} and
 730 normalized matching height $\xi = \gamma z_{match}$ in the upper part of the inner layer, we can match
 731 the Ekman profile to the inner layer by letting

$$\begin{aligned} u(z_{match}) &\equiv u_{match} = U_\infty + e^{-\xi} [A \cos \xi + B \sin \xi] \\ w(z_{match}) &\equiv w_{match} = W_\infty + e^{-\xi} [-A \sin \xi + B \cos \xi] \end{aligned} \quad (22)$$

$$\Rightarrow \begin{pmatrix} u_{match} - U_\infty \\ w_{match} - W_\infty \end{pmatrix} = e^{-\xi} \begin{pmatrix} A \\ B \end{pmatrix} \begin{pmatrix} \cos \xi & + \sin \xi \\ -\sin \xi & + \cos \xi \end{pmatrix} \quad (23)$$

$$(24)$$

733 Matching the profile at $\xi = 0$, one obtains $A = \Delta u_{\text{match}}$ and $B = -\Delta w_{\text{match}}$; and when the
 734 direction Ox is aligned with the geostrophic wind, we obtain the textbook-case $A = |\mathbf{G}|$ and
 735 $B = 0$.

736 Otherwise, choosing $B \neq 0$ allows to introduce a phase shift of the Ekman rotation with
 737 respect to the decay of the wind spiral. As, however, in our context, the thickness and position
 738 of the spiral can already be controlled by the eddy viscosity and an offset in ζ , here we let
 739 $B = 0$.

740 B Matching the spanwise velocity profiles in the inner layer

741 The spanwise profile in vicinity of the surface is given by $V/G = f_{V,\text{visc}}\delta^+$ with

$$f_{V,\text{visc}} = v_{\text{ref}} (\omega_v z^+ - 1 + e^{-\omega_v z^+}) \quad (25a)$$

$$f_{V,\log} = a_{\log} + b_{\log} \log z^+ + c_{\log} z^+ \quad (25b)$$

742 Matching the profiles and gradient $z_0 = 10^+$ and the value at $z_1 = 0.3\delta^+$ yields

$$v_{\text{ref}} (\omega_v z_0 + e^{-\omega_v z_0}) = v_0 = a_{\log} + b_{\log} \log z_0 + c_{\log} z_0 \quad (26a)$$

$$v_1 = a_{\log} + b_{\log} \log z_1 + c_{\log} z_1 \quad (26b)$$

$$v_{\text{ref}} \omega_z (1 - e^{-\omega_z z_0}) = d_0 = \frac{b_{\log}}{z_{10}} + c_{\log} \quad (26c)$$

743 The gradient condition implies $b_{\log} = (d_0 - c_{\log})z_0$, and yields

$$v_0 - z_0 d_0 \log z_0 = a_{\log} + c_{\log} (z_0 - z_0 \log z_0) \quad (27a)$$

$$v_1 - z_0 d_0 \log z_1 = a_{\log} + c_{\log} (z_1 - z_0 \log z_0) \quad (27b)$$

$$\Rightarrow c_{\log} = \frac{\Delta v - z_0 d_0 \log z_1 / z_0}{\Delta z} \quad (27c)$$

744 with $\Delta z = z_1 - z_0$ and $\Delta v = v_1 - v_0$. Then, the coefficient a_{\log} is estimated as

$$a_{\log} = v_0 - z_0 d_0 \log z_0 - \frac{\Delta v - z_0 d_0 \log z_1 / z_0}{\Delta z} [z_0 - z_0 \log z_0]. \quad (27d)$$

745 We note that $\log(z_1/z_0)/(z_1 - z_0) \rightarrow 0$ for large z_1 , and as $z_1 = 0.3\delta^+$, this implies that the
 746 second term in c_{\log} only plays a role at low and intermediate Re . Then, a_{\log} can be estimated
 747 as

$$a_{\log} \simeq v_0 - z_0 \left[d_0 \log z_0 - \frac{\Delta v}{\Delta z} (1 - \log z_0) \right] \quad (27e)$$

748 for large Re .

749 A Old Stuff

750 [OLD FROM HERE] Below this region, the gradients in span-wise velocity are rather small and
 751 the span-wise velocity monotonically approaches its surface boundary condition $V(z = 0) = 0$.
 752 While the streamwise velocity follows a universal inner scaling that has acquired its universal,
 753 Re -independent shape for $Re_D > \mathcal{O}(10^3)$, the span-wise component that defines how the
 754 velocity vector veers when the surface is approached, does not collapse in inner units, and
 755 there is, most importantly no sign of convergence even at the highest Reynolds numbers for
 756 which simulations were carried out. Even though the simplest assumption $V = 0$ is reasonable
 757 for the lower part of the surface surface layer ($z^- < 10^{-3}$), it does not appropriately capture
 758 the profile in the rest of the surface layer.

759 First, $V = 0$ implies a discontinuity in the velocity profile at $z^- = 0.1$, where the outer
 760 scaling found above yields a finite value at geophysical Re , i.e. there is non-zero veering in

761 the upper part of the surface layer—as is well-known also from field observation. Second, the
 762 layer around $z^- = 0.1$ is crucial to obtain the characteristic and well-established shape of the
 763 hodographs as the layer where V sets in marks the 'maximum' of V^- vs. U^- .

764 The scale for the magnitude of the span-wise velocity component is $u_* \sin \alpha$. Based on our
 765 DNS data, we suggest that the Reynolds number scaling of this velocity-magnitude scale is
 766 captured by $Re_\tau^{-1/2}$ which is indeed known from the generalization of higher-order statistics,
 767 such as turbulent fluxes in the inner layer (Marusic et al. 2013) that also follow a mixed scaling
 768 in the inner layer. We then parameterize the spanwise velocity at 10 wall units as anchor point
 769 in the inner layer:

$$V_{10} \equiv V(z^+ = 10) = 750 \frac{u_* \sin \alpha}{\sqrt{Re_\tau}}. \quad (28a)$$

770 This leaves us with three fixed points of the velocity profile in the inner layer, namely (i) the
 771 boundary condition $V_0 = 0$, (ii) V_{10} at $z^+ = 10$, and (iii) the lower end of the logarithmic
 772 profile at $z^- = 0.1$ where the latter two are semi-empirically estimated from DNS data. In
 773 absence of well-established scaling considerations for the span-wise velocity, the choice of profile
 774 fits joining these three points is indeed arbitrary, but we can resort to the DNS data for an
 775 empirical approach and find that a square-root profile fits $V(z^+)$ in the surface layer. A linear
 776 profile for V is employed in the viscous sub-layer. Based on the physical extent of the viscous
 777 sub-layer in Ekman flow around five wall units (Foken 2002; Ansorge 2019), we choose $z^+ = 5$
 778 to transition from one to the other and note that V is already very small at this height. The
 779 span-wise velocity profile in the surface layer is then estimated as

$$V(z^+) \Big|_{\text{inner}} = \begin{cases} a_1 z^+ & ; z^+ \leq 5 \\ b_1 + b_2 \sqrt{z^+} & ; 5 < z^+ < Re_\tau/10 \end{cases}, \quad (28b)$$

780 with b_1 and b_2 estimated such that

$$\begin{aligned} V(z^+ = 10) \Big|_{\text{inner}} &= V_{10} \\ V(z^+ = Re_\tau/10) \Big|_{\text{inner}} &= V_{\text{outer}}(0.1) \end{aligned} \Rightarrow \begin{cases} b_2 = \frac{V_{\text{outer}}(0.1) - V_{10}}{\sqrt{Re_\tau/10} - \sqrt{10}} \\ b_1 = V_{10} - \sqrt{10}b_2 \end{cases} \quad (28c)$$

781 We then estimate α from the matching condition at $z^+ = 5$, i.e.

$$5a = b_1 + \sqrt{5}b_2 \Rightarrow a = \frac{1}{5} \left[V_{10} + (\sqrt{5} - \sqrt{10}) \left(\frac{V_{\text{outer}} - V_{10}}{\sqrt{Re_\tau/10} - \sqrt{10}} \right) \right]. \quad (28d)$$

782 *Matching region.* While the profile composed of $V_{\text{inner}}(z^+ \leq 0.1Re_\tau)$, $V_{\text{outer}}(z^- > 0.1)$ is
 783 continuous, it is not smooth at $z^- = 0.1$, i.e. at the transition from power-law ($V \propto \sqrt{z^+}$)
 784 to logarithmic scaling. To alleviate this issue, we use a second-order polynomial for transition
 785 from the inner to the outer layer in the range $z_{\text{low}} < z < z_{\text{up}}$ such that

$$V_{\text{trans}}(z^-) = V_{\text{inner}}(z_{\text{low}}^+) + \Delta V (az_{\text{arg}} + b(z_{\text{arg}})^2) \quad (28e)$$

786 with $\Delta V = V_{\text{outer}}(z_{\text{up}}^-) - V_{\text{inner}}(z_{\text{low}}^+)$ and $z_{\text{arg}} = (z - z_{\text{low}})/(z_{\text{up}} - z_{\text{low}})$. It is $a + b = 1$ for
 787 $V_{\text{trans}}(z_{\text{up}}^-) = V_{\text{outer}}(z_{\text{up}}^-)$, and we constrain a by

$$\frac{\partial V_{\text{trans}}}{\partial z^-} \Big|_{z=z_{\text{low}}} = \frac{\partial V_{\text{inner}}}{\partial z^-} \Big|_{z=z_{\text{low}}}, \quad (28f)$$

788 where we find that $z_{\text{low}}^- = 0.06$ and $z_{\text{up}}^- = 0.13$ yield satisfactory agreement with DNS data.